HAL
open science

Giant exchange bias effect in Ruddlesden-Popper oxides SrLaFe0.25+xMn0.25Co0.5–xO4 (x=0,0.25): Role of the cluster glass magnetic phase in a quasi-two-dimensional perovskite

Anusree V. K, Ranjana R Das, P Neenu Lekshmi, Ramchandra Dhal, Claire Colin, P N Santhosh

To cite this version:

Anusree V. K, Ranjana R Das, P Neenu Lekshmi, Ramchandra Dhal, Claire Colin, et al.. Giant exchange bias effect in Ruddlesden-Popper oxides SrLaFe0.25+xMn0.25Co0.5–xO4 (x=0,0.25): Role of the cluster glass magnetic phase in a quasi-two-dimensional perovskite. Physical Review B, 2020, 102 (13), pp.134405. 10.1103/physrevb.102.134405 . hal-04147068

HAL Id: hal-04147068

https://hal.science/hal-04147068v1

Submitted on 30 Jun 2023

HAL is a multi-disciplinary open access archive for the deposit and dissemination of scientific research documents, whether they are published or not. The documents may come from teaching and research institutions in France or abroad, or from public or private research centers.

L'archive ouverte pluridisciplinaire **HAL**, est destinée au dépôt et à la diffusion de documents scientifiques de niveau recherche, publiés ou non, émanant des établissements d'enseignement et de recherche français ou étrangers, des laboratoires publics ou privés.

Giant exchange bias effect in Ruddlesden-Popper oxides $SrLaFe_{0.25+x}Mn_{0.25}Co_{0.5-x}O_4$ ($x = 0,\ 0.25$): Role of the cluster glass magnetic phase in a quasi-two-dimensional perovskite

Anusree V. K.,[1] Ranjana R. Das,[2] P. Neenu Lekshmi,[1,*] Ramchandra Dhal,[1] Claire V. Colin,[2] and P. N. Santhosh[1,†]
[1]*Department of Physics, Indian Institute of Technology Madras, Chennai 600036, India*
[2]*Institut Néel - CNRS, 25 Avenue des Martyrs - BP 166, 38042 Grenoble cedex 9, France*

(Received 24 July 2020; revised 13 September 2020; accepted 15 September 2020; published 6 October 2020)

Structural and magnetic studies on $SrLa(Fe_{0.25}Mn_{0.25})Co_{0.5}O_4$ (FMC1) and $SrLaFe_{0.5}(Mn_{0.25}Co_{0.25})O_4$ (FMC2) reveal unusually large exchange bias behavior in these atomically disordered quasi-two-dimensional layered perovskites. Powder x-ray as well as neutron diffraction confirm tetragonal crystal structure with $I4/mmm$ space group for both the compounds. Magnetization measurements on FMC1 as well as FMC2 reveal short-range antiferromagnetic ordering around room temperature and frozen magnetic clusters at lower temperatures ($T < 23$ K for FMC1 and $T < 43$ K for FMC2). The random occupancy of mixed-valent magnetic ions (Fe^{3+}/Fe^{4+}, Mn^{3+}/Mn^{4+}, Co^{2+}/Co^{3+}) at the perovskite octahedral sites give rise to locally varying competing antiferromagnetic and ferromagnetic exchange interactions, resulting in low temperature frozen spin states. Giant exchange bias values of ∼6 and ∼9.5 kOe were observed for FMC1 and FMC2, respectively, at 2 K under an applied field of 50 kOe. In comparison, the Co-rich FMC1 exhibits higher magnetization and coercivity, whereas Fe-rich FMC2 possesses a higher exchange bias effect. Our experimental results reveal compositional tuning induced exotic magnetic behavior in quasi-two-dimensional layered oxides.

DOI: 10.1103/PhysRevB.102.134405

I. INTRODUCTION

Perovskites, well-known versatile oxides, have been explored rigorously with different combinations of magnetic rare earth and transition metal ions. In the list of multifunctional materials, perovskites lead because of their diverse physical properties such as magnetoresistance, multiferroic properties, magnetocaloric effect, exchange bias (EB), etc. [1–4]. However, in recent years, quasi-two-dimensional (2D) layered perovskite systems are investigated in connection with their strongly correlated d electrons, and the mixed-valence states of the transition-metal ions owing to the promising experimental results in comparison to its 3D perovskite [5]. One such category of quasi-2D layered perovskite is the Ruddlesden-Popper (RP) series $[(A'/AO)(ABO_3)_n]$ where A' = alkaline earth ion, A = rare earth ion, B = transition metal ion, O = Oxygen ion, and n (1,2,3, …) represents the number of perovskite layers intercalated between two A'O layers in a unit cell [6]. The quasi-dimensionality originates due to the separation of perovskite blocks along the long crystallographic axis (c axis) by nonmagnetic A/A′O layers. Crystal structure of n layered RP series can be visualized as BO_6 octahedral blocks sandwiched between $A/A'O$ layers, with n number of BO_6 sheets in each octahedral block. So, for single-layered RP compounds ($n = 1$) in Fig. 1(a), there will be one connected BO_6 sheet in the ab plane, which is sandwiched between adjacent A/A'O layers as shown in Fig. 1(b).

Inhomogenous magnetic phases in atomically disordered perovskites lead to coexistence of ferromagnetic (FM) and antiferromagnetic (AFM) interactions resulting in magnetic frustrations [7]. These competing magnetic exchange interactions give rise to an interesting magnetic phenomenon known as EB. The EB effect is usually associated with a horizontal and/or vertical shift in hysteresis loops as a result of unidirectional anisotropy at the FM/AFM interfaces [8,9]. In addition, EB has been investigated in many perovskites consisting of interfaces of frozen magnetic phases such as FM/spin glass, AFM/spin glass and ferrimagnetic/spin glass [10–12]. The EB effect is technologically important and has been implemented in nonvolatile memory, giant magnetoresistance sensors, and magnetic read heads [13–16]. Similar to perovskites, the properties of RP oxides are also strongly influenced by structural distortions and atomic disorder. However, in comparison with perovskites, quasilayered perovskite systems are not much explored for EB effects.

Recently, our group reported a giant EB field of ∼5.5 kOe in the single-layered RP system $SrLaCo_{0.5}Mn_{0.5}O_4$ (SLCMO), for which a low temperature glassy magnetic transition ($T_{C2} \sim 50$ K) along with a ferromagnetic phase transition (at $T_{C1} \sim 150$ K) were observed [17]. The perovskite analog of SLCMO is La_2CoMnO_6, which is a FM double perovskite. The observation of giant EB in SLCMO was explained in terms of competing FM and AFM interactions at nanoscale domains along the perovskite layers. In the present work, we have considered a RP oxide $SrLaFe_{0.5}Co_{0.5}O_4$, where the perovskite analog is

*Present address: IFIMUP-IN Material Physics Institute of the Univ. of Porto, Institute of Nanoscience and Nanotechnology, Rua do Campo Alegre, 687, 4169-007 Porto, Portugal.
†Author to whom correspondence should be addressed: santhosh@iitm.ac.in

 ©2020 American Physical Society

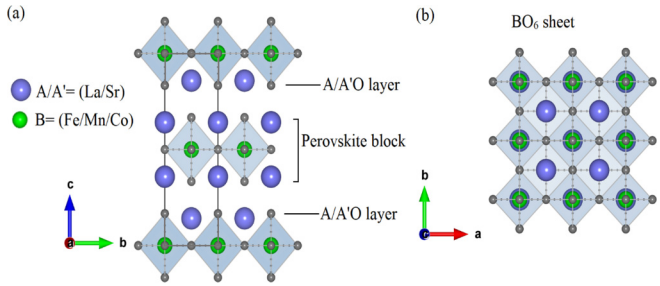

FIG. 1. (a) Single layered Ruddlesden-Popper crystal structure with A/A' (La/Sr) and B (a combination of Fe/Mn/Co) in a crystallographic two unit cells (one unit cell is represented as black solid line) with *I4/mmm* space group which viewed along the a axis. (b) The view of BO_6 octahedral sheets, which are connected three dimensionally, in the *ab* plane.

La_2FeCoO_6, which is an AFM double perovskite [18]. Moreover, very recently EB effects and glassy magnetic phase has been reported for the double perovskite $LaSrFeCoO_6$ [19]. Since we are focused on FM/AFM interfaces and EB effect, we have designed two quasi-2D layered compounds by introducing Mn ions in the perovskite layer of $SrLaFe_{0.5}Co_{0.5}O_4$, in order to enhance the FM contribution and magnetic inhomogeneity. Thus, the present work gives a comparative study on the impact of Mn ions on the structural and magnetic features of Co-rich compound $SrLaFe_{0.25}Mn_{0.25}Co_{0.5}O_4$ and Fe-rich compound $SrLaFe_{0.5}Mn_{0.25}Co_{0.25}O_4$. In-depth analysis using DC and AC magnetic measurements together with neutron powder diffraction and heat capacity analysis confirm lower temperature cluster glass phase in both the compounds wherein $SrLaFe_{0.5}Mn_{0.25}Co_{0.25}O_4$ exhibit a higher EB effect.

II. EXPERIMENTAL DETAILS

Polycrystalline single phase $SrLaFe_{0.25}Mn_{0.25}Co_{0.5}O_4$ (FMC1) and $SrLaFe_{0.5}Mn_{0.25}Co_{0.25}O_4$ (FMC2) were synthesized by citrate gel method. Stoichiometric amount of $La(NO_3)_3 \cdot xH_2O$, $Sr(NO_3)_2$, $Co(NO_3)_2 \cdot 6H_2O$, $Fe(NO_3)_3 \cdot 9H_2O$ were mixed in the required ratio as precursors to which $Mn(CH_3COO)_2 \cdot 4H_2O$ dissolved in dilute HNO_3 was added. This solution was stirred and heated on a hot plate up to 573 K. Citric acid and ethylene glycol were added for gel formation. After drying the gel, the dried mixture was then annealed at different temperatures ranging from 1173 to 1373 K with intermediate grindings. Structure and phase purity of the samples have been confirmed by x-ray diffraction (XRD) technique using Rigaku Smart Lab diffractometer with Cu-$K\alpha$ radiation ($\lambda = 1.5406$ Å) (2θ range of $10° - 90°$, in steps of 0.02° and a counting time of 1 s/step). Rietveld refinement of the obtained patterns was performed using FULLPROF suite software [20] and the crystallographic structure was constructed using VESTA [21]. X-ray photoelectron spectroscopy (XPS) was performed using Nexsa x-ray photoelectron spectrometer system by ThermoFisher Scientific. DC and AC magnetic characterizations were done using a magnetic properties measurement system, superconducting quantum interference device—vibrating sample magnetometer (Quantum Design). Temperature evolution of DC magnetization was performed from 350 K down to 5 K at different applied fields. Field cooled (FC) and zero field cooled (ZFC) hysteresis loops were recorded at several temperatures in the range ±70 kOe. Neutron powder diffraction measurement was performed at different temperatures from 2 to 500 K at crg-D1B/(ILL) [22] to detect the magnetic ordering. Temperature dependent heat capacity measurement was performed using a physical property measurement system (PPMS) from Quantum Design, USA.

TABLE I. Structural parameters of FMC1 and FMC2 obtained from Rietveld refinement of XRD histograms.

Space group	FMC1 *I4/mmm*	FMC2 *I4/mmm*
Lattice parameters		
a (Å)	3.8396(2)	3.8582(3)
c (Å)	12.5854(1)	12.6641(1)
Volume (Å^3)	185.547(3)	188.517(4)
La/Sr (x/ y/z)	0.0/0.0/0.3592(5)	0.0/0.0/0.3586(4)
Fe/Mn/Co (x/y/z)	0.0/0.0/0.0	0.0/0.0/0.0
O1 (x/ y/ z)	0.0/0.5/0.0	0.0/0.5/0.0
O2 (x/ y/ z)	0.0/0.0/0.1664(2)	0.0/0.0/0.1679(2)
Bond length (Å)		
La/Sr – O1 × 4	2.6127(2)	2.6322(2)
La/Sr – O2	2.4258(6)	2.4156(2)
La/Sr – O2 × 4	2.7341(4)	2.7486(2)
Fe/Mn/Co – O1 × 4	1.9198(3)	1.9291(2)
Fe/Mn/Co – O2 × 2	2.0947(3)	2.1255(3)
$\chi^2/R_{wp}/R_p$	3.18/2.24% /1.63%	4.26/2.99% /2.15%

III. RESULTS AND DISCUSSION

A. Crystal structure

Rietveld refinement on XRD patterns of polycrystalline FMC1 and FMC2 confirms single phase tetragonal structure with *I4/mmm* space group (139) wherein FMC2 has a 1.58% bigger unit cell volume than FMC1. This may be due to the higher content of Fe ion [ionic radius of Fe^{3+} (HS) = 0.645 Å], which has slightly higher ionic radius compared to Co ion [ionic radius of Co^{3+}(HS) = 0.61 Å], whereas Fe ion has equal ionic radius to the Mn ion [ionic radius of Mn^{3+} (HS) = 0.645 Å]. The refined lattice parameters, unit cell volume, atomic coordinates, and reliability factors of both samples are given in Table I; the equatorial and apical oxygens are represented as O1 and O2, respectively. Obtained refinement parameters are comparable with single-layered RP compounds [17,23]. The Rietveld refined XRD patterns for FMC1 and FMC2 are shown in Figs. 2(a) and 2(b), respectively.

As there are three transition metal ions present (Fe, Co, and Mn) at the B site, ionic radii, lattice parameters, unit cell volume and c/a ratio of a series of RP compounds $SrLaMO_4$ (B = Fe, Co, Mn in different ratios) having I*4/mmm* crystal structure, was plotted to understand the variation of their unit cell dimensions (Fig. 3). The compositions include, in the x axis of Fig. 3 from left, $SrLaCoO_4$, $SrLaFe_{0.5}Co_{0.5}O_4$, $SrLaFe_{0.25}Mn_{0.25}Co_{0.5}O_4$, $SrLaCo_{0.5}Mn_{0.5}O_4$, $SrLaFe_{0.5}Mn_{0.25}Co_{0.25}O_4$, $SrLaFeO_4$, and

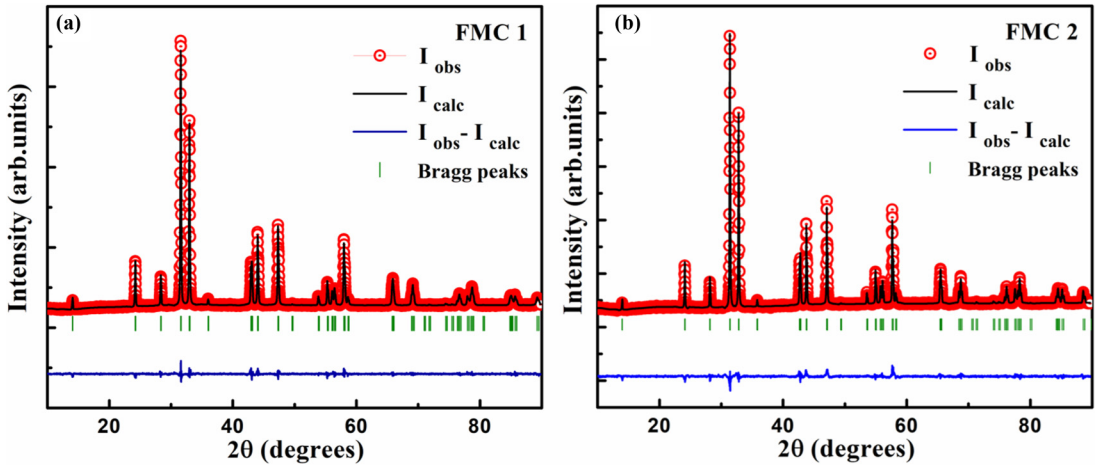

FIG. 2. Rietveld refined x-ray diffraction patterns obtained at room temperature for (a) FMC1 and (b) FMC2.

$SrLaMnO_4$ [17,24,25] based on the ionic radii value of six coordinated +3 charge states with HS state of transition metal ions from Shannon radii database [26]. The higher-end members of the series, $SrLaFeO_4$ and $SrLaMnO_4$ possess nearly similar values of unit cell volume [due to similar ionic radii of Fe^{3+} (HS) and Mn^{3+} (HS) ions], whereas the first member of the series $SrLaCoO_4$ has the lowest. The crystallographic parameters of $SrLaFe_{0.5}Co_{0.5}O_4$, $SrLaFe_{0.25}Mn_{0.25}Co_{0.5}O_4$, and $SrLaMn_{0.5}Co_{0.5}O_4$ remain almost similar due to the equal ionic radii of Fe and Mn. The lattice parameters a and c increase with the increase in ionic radii in the series whereas maximum elongated c axis and minimum a lattice constant were observed for Jahn-Teller distorted $SrLaMnO_4$. In $SrLaMnO_4$, the bond length of B-O1 is shorter and B-O2 is longer than the other members of the series as shown in the comparison in Fig. S1 in the Supplemental Material [27,75]. Except for $SrLaMnO_4$, c/a ratio was found ~3.28 for all the other compositions, which is a clear indication of tetragonal features according to crystallographic tetragonal symmetry of $I4/mmm$ space group. It is evident from the comparison curve that structural variation associated with the introduction of Mn ions on $SrLaFe_{0.5}Co_{0.5}O_4$ is controlled by the size of the ion that is being replaced (Fe in FMC1 and Co in FMC2).

B. X-ray photoelectron spectroscopy

X-ray photoelectron spectroscopy (XPS) was performed to obtain information about surface chemical states of the present compounds. Core level XPS spectra of Co, Fe, and Mn were analyzed to derive their oxidation states. Deconvoluted peaks of Co, Fe, and Mn $2p_{3/2}$ spectra are presented in Fig. 4 and the fitting of $2p_{1/2}$ lines are given in the Supplemental Material as Fig. S2, which clearly shows the coexistence of at least two oxidation states. From the fitting of Mn $2p_{3/2}$ spectra, binding energy values of 641.12, 642.83 eV and 641.18, 642.86 eV were observed for FMC1 and FMC2, respectively. These values correspond to Mn^{3+} and Mn^{4+} valence states in 60 and 40% [28]. Binding energies of the deconvoluted peaks of Co $2p_{3/2}$ spectra were obtained at 779.94 eV, 781.59 eV and 779.91 eV, 781.46 eV for FMC1 and FMC2, respectively. These values are following those of Co^{3+} and Co^{2+} valence states in 60:40% ratio [29]. In addition, two satellite peaks were observed at 786 and 803 eV for FMC1 as well as for FMC2, which further confirm the existence of Co^{2+} valence state (shown in the Supplemental Material Fig. S2b [75]) [30]. Similarly, deconvolution of Fe $2p_{3/2}$ spectral lines confirm the presence of Fe^{3+} and Fe^{4+}, with the binding energy values of ~710.22, ~712.65 eV and 710.3, ~712.72 eV for FMC1 and FMC2, respectively [31,32]. Further, satellite peaks observed in Fe core spectra around 717 and 731 eV in both compounds again confirm the presence of +3 oxidation state (shown in the Supplemental Material Fig. S2c [75]) [30,32,33]. The ratio of valence states Fe^{3+} : Fe^{4+} is 60:40% in FMC1 and 75:25% in FMC2. We conclude from XPS studies that the majority of Fe/Mn/Co spins are in +3 states. Further, in the magnetization studies, we will explain how multiple valence states of magnetic ions in these systems bring in the competing magnetic interactions leading to giant exchange bias below spin freezing temperature.

C. Thermal variation of DC magnetization

To investigate the intricate magnetic properties prognosticated from the magnetic B site ions having various valence states ($Fe^{3+/4+}$, $Co^{2+/3+}$, and $Mn^{3+/4+}$) and site disorder, temperature variation of magnetization measurements were performed. Figures 5(a) and 5(b) represent the thermal evolution of DC magnetization for FMC1 and FMC2, respectively, in the temperature range 5–350 K under ZFC and FC protocols at applied fields of 100 Oe and 50 kOe. The ZFC curves of both compounds show two transitions designated as T_1 and T_2, which are more clearly shown in the derivative curves [inset of Figs. 5(a) and 5(b)]. In both compounds, the lower temperature transition T_1 is more pronounced and is observed at 23 and 43 K for FMC1 and FMC2, respectively. The higher temperature transition T_2 is observed at 297 and 318 K for FMC1 and FMC2, respectively. For comparison, the magnetization curves of the parent compound $LaSrFe_{0.5}Co_{0.5}O_4$ at an applied field of 500 Oe was plotted and shown in the Supplemental Material (Fig. S3 [75]), which shows two transitions at 13 and 384 K. The $LaSrCoO_4$ layered compound, is reported as a spin glass with glassy magnetic transition at 7 K [34], in contrast, its 3D analog $LaCoO_3$ exhibits frustrated magnetic transition below 100 K [35]. The Fe-doped

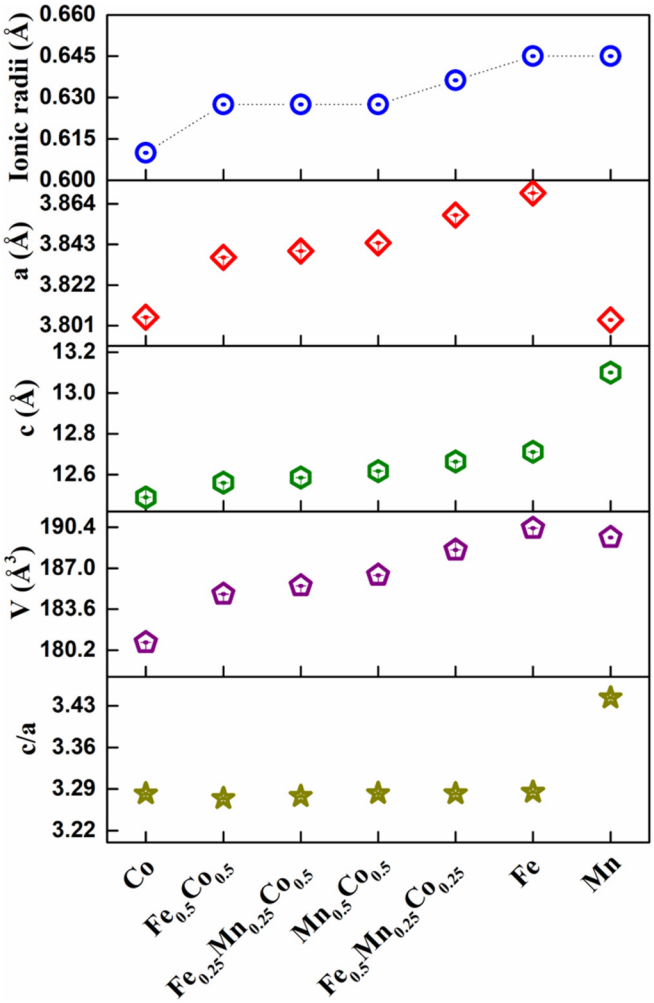

FIG. 3. From top to bottom, variation of ionic radii, lattice constant a(Å), lattice constant c(Å), lattice volume, and c/a ratio of $SrLaMO_4$ where M represents transition metal ions (M = Fe/Co/Mn) with different concentrations. Here the value of ionic radii of transition metal ions with 3+ charge states in six coordinated high-spin state are considered from the database of Shannon ionic radii.

layered compound, $LaSrCo_{1-x}Fe_xO_4$, is reported with disordered Co/Fe distribution wherein the lower concentration of Fe shows coexistence of FM state with a glassy magnetic state whereas AFM interaction dominates for higher Fe concentration [36]. $LaSrFeO_4$ is reported with short-range magnetic clusters below 400 K [37], whereas the 3D analog $LaFeO_3$ is reported to have AFM transition at 740 K [38]. The RP structured perovskites usually exhibit a huge reduction in magnetic ordering temperature compared to their 3D analog. The reason is the absence of 3D magnetic exchange network in RP compounds due to ½ unit cell displacement of perovskite blocks in the [110] direction, leading to a quasi-2D structure. Thus, the higher temperature T_2 transition in FMC1 and FMC2 might be an AFM transition due to the Fe^{3+}-O-Fe^{3+} AFM superexchange interactions. The higher transition temperature in FMC2 (318 K) compared to FMC1 (297 K) might be the influence of more Fe-rich regions in FMC2 with dominating Fe^{3+} ions.

The irreversibility between ZFC and FC magnetization points towards the possibility of magnetic frustrations at lower temperatures. In the present compounds, the disordered perovskite layers, with different magnetic ions in multivalent states ($Fe^{3+/4+}$, $Co^{2+/3+}$, and $Mn^{3+/4+}$), possess inhomogeneous magnetic phases due to the coexistence of AFM and FM interactions. Among the possible magnetic exchange interactions, Fe involving exchange interactions are predominantly AFM and possess magnetic ordering at higher temperatures [18,39] except for Fe^{3+}-O-Co^{3+} [wherein Co^{3+} ions will be in the low-spin state (t_{2g}^6, e_g^0)] and Fe^{3+}-O-Mn^{4+} interactions, which are FM interactions [40,41]. Further, Co^{3+}-O-Mn^{4+}, Mn^{4+}-O-Mn^{4+}, Mn^{3+}-O-Mn^{3+} and Co^{3+}-O-Co^{3+} also contribute to AFM interaction, whereas FM coupling arises from Co^{2+}-O-Mn^{4+}, Co^{3+}-O-Mn^{3+} and Mn^{3+}-O-Mn^{4+} [42,43]. Usually, competing AFM-FM magnetic interactions introduce magnetic frustrations leading to a low temperature spin frozen state such as a spin glass or cluster glass state [44–46]. Thus, the T_1 transition observed in the present compounds can be considered as a glassy magnetic transition that requires further detailed experimental evidence. The dissimilarity in ZFC-FC bifurcation between the compounds along with much higher T_1 transition observed for FMC2 (43 K under 100 Oe) compared to that in FMC1 (23 K under 100 Oe), will be discussed later after categorizing the T_1 transition.

D. Magnetic memory effect

To discern the origin of glassy behavior, predicted from the DC magnetization data, magnetic memory measurements were carried out under stop and wait protocol [47–49]. In ZFC protocol, we followed the conventional method of cooling the sample in the absence of magnetic field with intermediate halts. Initially, the sample was zero field cooled from 350 K down to 5 K at a rate of 1 K/min without any intermediate halt. Further, the $M_{\mathrm{ZFC}}^{\mathrm{Reference}}$ data was recorded during the warming cycle at the same rate in the presence of a small applied field of 100 Oe. To get the memory magnetization curve ($M_{\mathrm{ZFC}}^{\mathrm{Memory}}$), again the sample was zero field cooled down to 5 K at the same rate with an intermediate halt at $T < T_1$ (10 K for FMC1 and 30 K for FMC2) for 3 h; the data was recorded during the warming cycle (in the presence of a small applied field of 100 Oe) without any halts. Figures 6(a) and 6(b) represent the temperature response of $M_{\mathrm{ZFC}}^{\mathrm{Reference}}$ and $M_{\mathrm{ZFC}}^{\mathrm{Memory}}$ along with the difference curves for FMC1 and FMC2, respectively. In the FC protocol, initially the sample was cooled from 350 K down to 5 K (1 K/min) in the presence of an applied field of 100 Oe. The data taken during the subsequent warming up to 200 K is labeled as $M_{\mathrm{FCW}}^{\mathrm{Reference}}$. Again, the sample was cooled down in the same rate to 5 K in the presence of 100 Oe field, interrupted by a halt at 10 and 30 K for FMC1 and FMC2, respectively, for 3 h. The applied magnetic field (100 Oe) is switched off during the halt period after which the field is turned on and the cooling is continued down to 5 K. The corresponding FC curve labeled as $M_{\mathrm{FCC}}^{\mathrm{Stop}}$ exhibits a steplike feature at the halt temperatures. As 5 K is attained, the sample is again heated to 300 K continuously at the same rate and the data obtained during this warming cycle is represented by the $M_{\mathrm{FCW}}^{\mathrm{memory}}$ curve. FC memory curves obtained

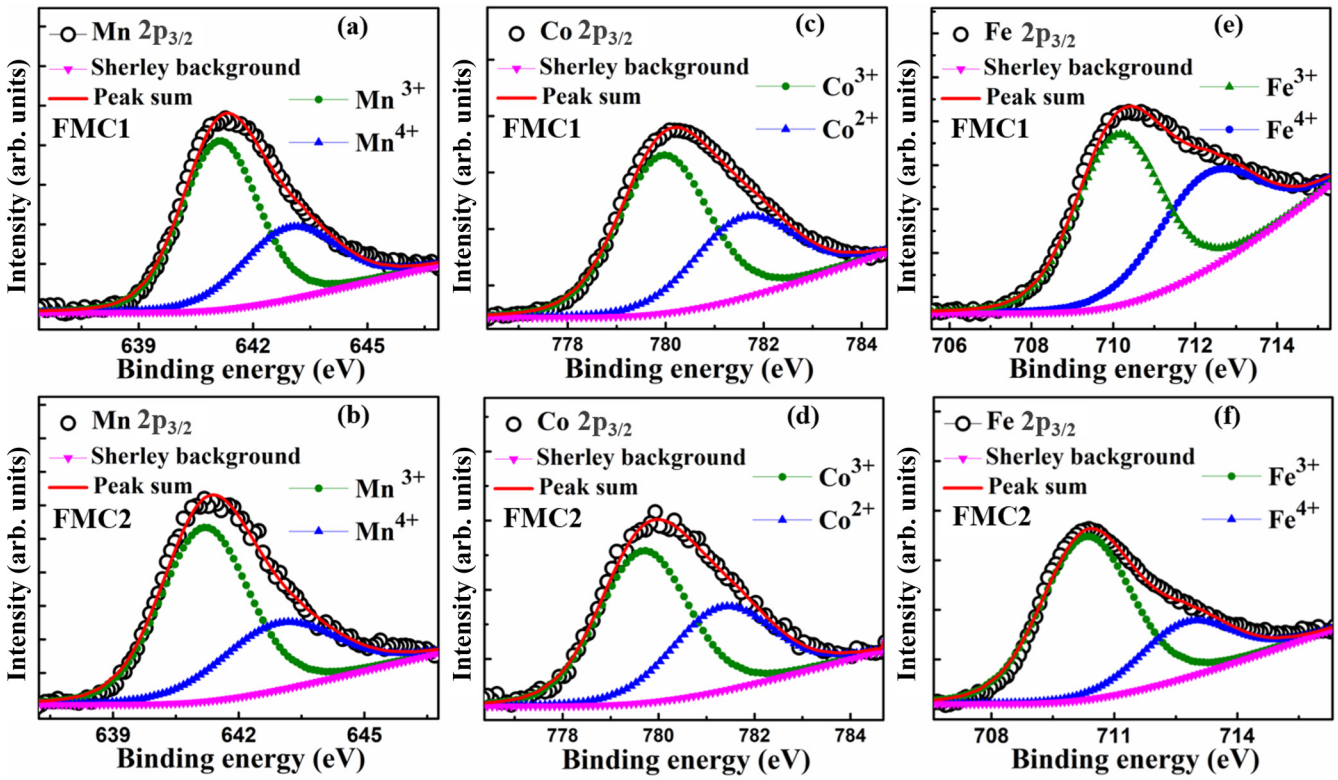

FIG. 4. $2p_{3/2}$ XPS spectra of Mn, Co, and Fe ions of FMC1 in the top row (a), (c), (e), and those of FMC2 in the bottom row, (b), (d), (f).

for FMC1 and FMC2 are depicted in Figs. 6(c) and 6(d), respectively.

The presence of sharp memory dips in the difference curves of ZFC memory, the steplike feature in $M_{\mathrm{FCC}}^{\mathrm{Stop}}$ and kinks near the halt temperatures in the $M_{\mathrm{FCW}}^{\mathrm{memory}}$ curve confirms the presence of glassy magnetic phase below T_1 in both FMC1 and FMC2. We have also employed a stop for 3 h at 150 K ($T > T_1$) during FC memory in FMC1 as well in FMC2, which is also portrayed in Figs. 6(c) and 6(d). However, no memory features were observed at 150 K in both cases. Thus, the memory effect shows that, in both compounds, the coexisting AFM-FM interactions are competing more prominently below T_1, resulting in glassy magnetic ground states.

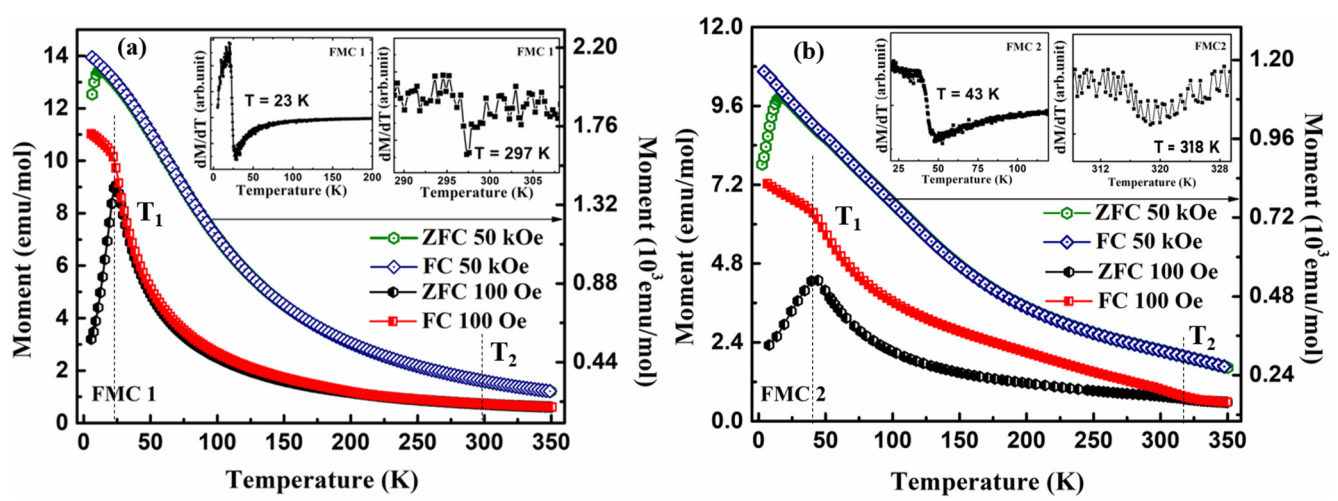

FIG. 5. Thermal response of magnetization at applied fields of 100 Oe and 50 kOe for (a) FMC1 and (b) FMC2. Both ZFC and FC curves are shown. Observed low temperature and high temperature transitions are represented as T_1 and T_2, respectively. Derivative curves, dM/dT vs T near the transitions are given in the insets.

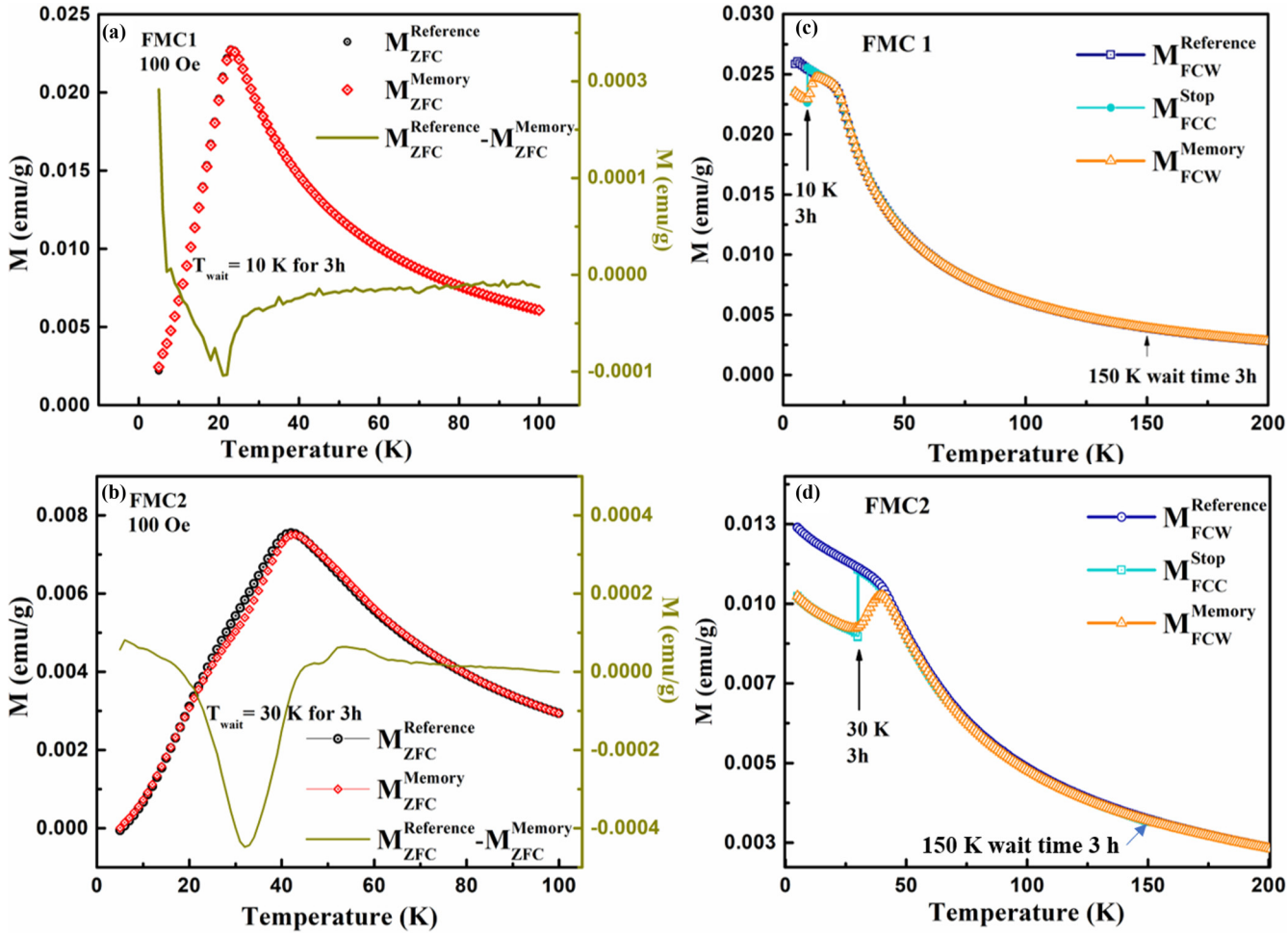

FIG. 6. Temperature response of memory effect under ZFC protocol in (a) FMC1 and (b) FMC2. (c) and d) represent the same under FC protocol in FMC1 and FMC2, respectively. Halt temperatures of 10 and 30 K were employed in FMC1 and FMC2, respectively.

E. AC susceptibility

In order to characterize the nature of the glassy magnetic state in FMC1 and FMC2 below glassy transition temperature T_1, confirmed from the memory effect, a temperature dependent AC susceptibility measurement, χ (T), was performed in the low temperature regime at various frequencies under an AC drive field of 4 Oe. The maxima observed in the real part of susceptibility, χ'(T) around 27.5 and 48.2 K for FMC1 and FMC2, respectively, at 123 Hz, shown in Figs. 7(a) and 7(b), corroborates the T_1 peak in the DC magnetization curves. Also, a systematic peak shift to higher temperature was observed as the measuring frequency increases from 123 to 999 Hz, which further confirms the existence of a glassy magnetic phase. Thus to understand the spin freezing dynamics, the Mydosh parameter was examined followed by Vogel-Fulcher (VF) and critical slowing dynamics models.

The Mydosh parameter has been used as a criterion to categorize the glassy magnetic systems according to the response of magnetic spins to the applied frequency (relative shift in peak temperature). The Mydosh parameter, defined as $K = \frac{\Delta T_P}{T_P\ \Delta(\log f)}$, where T_p represents the temperature where the peak/maximum value of AC susceptibility occurs and f is the measured frequency, was found to be 0.06 and 0.05 for FMC1 and FMC2, respectively. The values obtained characterize that both compounds are more likely a cluster glass type for which $K \leqslant 0.08$ is usually reported [17,50]. Further, to understand the interaction among the frozen spin clusters, the Vogel-Fulcher (VF) relaxation model was adopted and the fitting is shown in Figs. 7(c) and 7(d) for FMC1 and FMC2, respectively. According to VF model, a magnetic system containing interacting particles (or spin clusters) undergoes a relaxation process in which the relaxation time follows the VF law

$$\tau = \tau_0 \exp\left[\frac{-E_A}{k_B(T_P - T_{VF})}\right], \tag{1}$$

where τ is the relaxation time, E_A is the activation energy, τ_0 is the characteristic time between the relaxation attempts of spin clusters, and T_{VF} is the VF temperature, which gives a qualitative measure of the interaction between the clusters. Best fit was obtained with $\tau_0 = 1.74 \times 10^{-4}$ s, $T_{VF} = 27.08 \pm 0.53$ K for FMC1 and $\tau_0 = 4.43 \times 10^{-4}$ s, $T_{VF} = 45.82 \pm 0.11$ K for FMC2. The characteristic relaxation time obtained from VF fitting is much larger than that of typical spin glass systems. This indicates the presence of interacting magnetic clusters in both FMC1 and FMC2 [51]. Additionally, we have fitted the data with critical slowing down

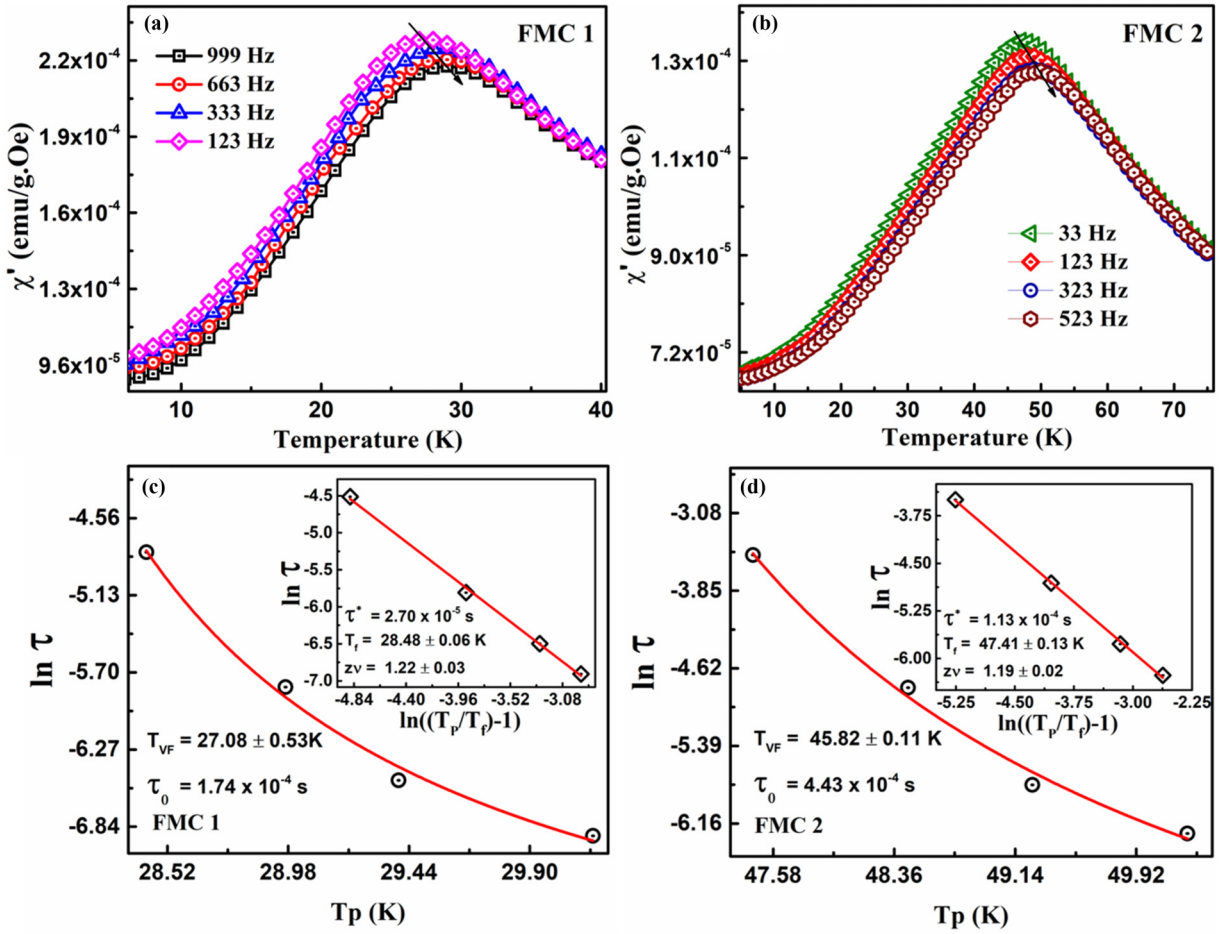

FIG. 7. Temperature response of real part of AC susceptibility χ' of (a) FMC1 and (b) FMC2 at different measuring frequencies. Arrow indicates the variation in the peak value of ac susceptibility (T_P) with increase in frequency. (c) and (d) represent the V-F fitting of FMC1 and FMC2, respectively. Critical slowing dynamics model fit (solid red line) is shown in the insets of both (c) and (d). Fitted parameters are also mentioned in the figures.

dynamics given by (according to the dynamic scaling theory),

$$\tau = \tau^* \left[\frac{(T_P - T_f)}{T_f} \right]^{-z\nu}, \tag{2}$$

where τ^* is the characteristic relaxation time of the individual spin cluster, T_f is the freezing temperature, and $z\nu$ is the dynamic critical exponent [52–54]. Here the relaxation time τ follows a power law derived from the proportionality, $\tau \propto \xi^z$, where ξ is the correlation length between the spin clusters ($\xi \propto [\frac{T_p}{T_f} - 1]^{-\nu}$) [53]. According to dynamic scaling theory, relaxation time (as well as the correlation length) diverges as the freezing temperature T_f is approached from high temperature side [55]. Fitted curves and obtained parameters are given in the inset of Figs. 7(c) and 7(d) for FMC1 and FMC2, respectively. Obtained values of the characteristic relaxation τ^*, $z\nu$ and T_f are 2.70×10^{-5}, 1.22 ± 0.03, 28.48 ± 0.06 and 11.3×10^{-5}, 1.19 ± 0.02, 47.41 ± 0.13 for FMC1 and FMC2, respectively. Satisfactory fitting of the data was obtained using VF model as well as critical slowing down dynamics model for both FMC1 and FMC2. Also, the large values obtained for spin relaxation time (τ_0 and τ^*) confirm interacting frozen spin clusters at lower temperatures ($<T_1$) in both FMC1 and FMC2 [56] whereas noninteracting frozen spins involving spin glass systems usually exhibit very fast relaxation time (10^{-10}–10^{-13} s). [51,52,57]. Thus, VF and critical slowing down dynamics models along with the Mydosh parameter strongly support cluster glass behavior in both FMC1 and FMC2 below T_1 transition.

Below T_1 transition, both the compounds enter into a spin frustrated frozen state when the coexisting FM and AFM exchange interactions become competing. Earlier we have noted that the T_1 transition for FMC2 is observed at a much higher temperature (43 K under 100 Oe) compared to FMC1 (23 K under 100 Oe). Moreover, the ZFC and FC bifurcation starts from T_1 in FMC1 whereas the irreversibility between ZFC and FC curves of FMC2 persists above T_1 (as clearly seen in the M-T curves at 100 Oe). Also, in both the compounds under the higher applied field, the ZFC and FC bifurcation decreases to lower temperature and T_2 transition vanishes. This suggests T_2 transition in both compounds is a short-range Fe-O-Fe AFM ordering. However, the cluster glass transition at a comparatively higher temperature ($T_1 = 43$ K) in FMC2 along with its ZFC and FC bifurcation ($T < T_2$) under lower applied

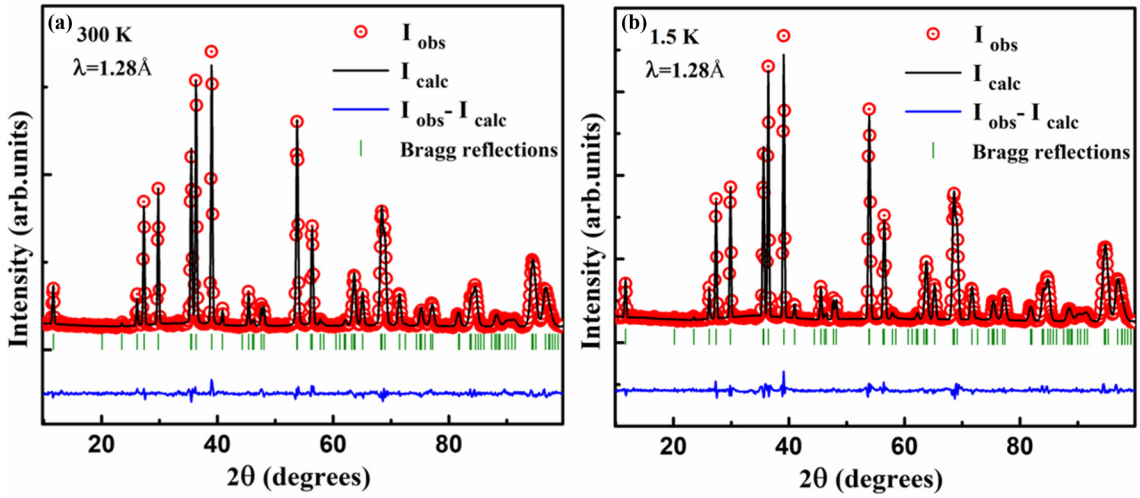

FIG. 8. Powder neutron diffraction patterns of FMC2 at (a) 300 K and at (b) 1.5 K. Observed, calculated, and the difference patterns are given along with the allowed Bragg reflections.

field points to the existence of fairly strong competing AFM-FM interactions even above T_1 in FMC2. Such a peculiar magnetic feature observed in FMC2 might be due to the existence of more Fe-rich regions with AFM (Fe^{3+}-O-Fe^{3+} and Fe^{3+}-O-Mn^{3+}) and FM (Fe^{3+}-O-Mn^{4+}) interactions, which usually exhibit magnetic ordering at higher temperatures [40,58,59]. Such strong AFM-FM competing interactions are absent above T_1 in FMC1 due to dominant Co-rich regions, where the corresponding superexchange interactions may lead to the formation of a spin glass state at low temperature [34].

F. Neutron diffraction

Temperature evolution of neutron powder diffraction (NPD) ($\lambda = 1.28$ Å) was performed on FMC2 in the temperature range 1.5 K to 500 K as FMC2 has more Fe-rich regions and the T_2 peak is prominent in FMC2. The collected NPD patterns confirm tetragonal crystal structure with *I4/mmm* space group Rietveld refinement was carried out on the collected patterns and satisfactory reliability factors were obtained. The observed patterns at 300 and 1.5 K, along with calculated (using *I4/mmm* space group) and difference patterns resulted from the refinement process are shown in Figs. 8(a) and 8(b), respectively. To be specific, the signature of the Fe-Fe AFM ordering (T_2) and diffuse magnetic scattering remain undetected by NPD, which further confirms the cluster size to be very small. Details of the crystal structure parameters obtained from the Rietveld refinement of NPD at 1.5, 300, and 500 K are listed in the Supplemental Material [75].

G. Heat capacity

Figures 9(a) and 9(b) depict the temperature response of specific heat capacity C_P (T), for FMC1 and FMC2, respectively, measured at zero field ($H = 0$) in the temperature range 2–200 K. Presence of glassy magnetic nature at low temperature is further evidenced from the detailed analysis of the temperature variation of C_P data at low temperature. C_P/T vs T^2 plots for both the compounds [shown as inset (I) of Figs. 9(a) and 9(b)] exhibit a nonlinear behavior at low temperature, deviating from $C_p = \gamma T + \beta T^3$ behavior, where the first term, linear with temperature, represents the electronic contribution and the second term represents the lattice contribution towards heat capacity. The negative curvature observed in C_P/T vs T^2 plots indicates the presence of a magnetic contribution to heat capacity. The coefficient of electronic contribution γ, which is proportional to the density of states at the Fermi level, was found to be negative for both FMC1 and FMC2 indicating very low electrical conductivity at low temperature [60]. The addition of a magnetic term $\delta T^{3/2}$, which is typical for spin glass or ferromagnetic systems [60–63], improved the fit (inset II of Figs. 9(a) and 9(b)) and the obtained coefficients are $\delta = 18.62 \pm 0.55$ mJ mol^{-1} K$^{-5/2}$ and $\delta = 7.59 \pm 0.48$ mJ mol^{-1} K$^{-5/2}$ for FMC1 and FMC2, respectively. The term $T^{3/2}$ indicates the presence of FM clusters in both FMC1 and FMC2. The coefficient of lattice contribution β, obtained from the fit are 0.34 ± 0.02 and 0.17 ± 0.01 mJ mol^{-1} K^{-4} for FMC1 and FMC2, respectively. The Debye temperature was determined from β using $\theta_D = [\frac{12\pi^4 nR}{5\beta}]^{1/3}$, where n is the number of atoms per formula unit cell, and R is the universal ideal gas constant. The calculated values of the Debye temperature are $\theta_D = 225.29$ K for FMC1 and $\theta_D = 283.85$ K for FMC2. Higher value of θ_D in FMC2 may be correlated with hardening of lattice vibrations due to dominating AFM interactions [60]. Therefore, the analysis of heat capacity data along with DC and AC magnetization concludes that both the compounds (FMC1 and FMC2) exhibit glassy magnetic state at lower temperatures below T_1.

H. Isothermal magnetization and Exchange bias

Isothermal field dependent magnetization measurements, M(H), under ZFC protocol were carried out on both FMC1 and FMC2 samples in the field range ±70 kOe at temperatures 5, 75, and 350 K, as shown in Fig. 10. Unsaturated loops at 5 K even for the maximum applied field of 70 kOe indicates the presence of competing magnetic phases in the compounds (FM/AFM/cluster glass). At 5 K, maximum magnetization obtained under an applied field of 70 kOe is

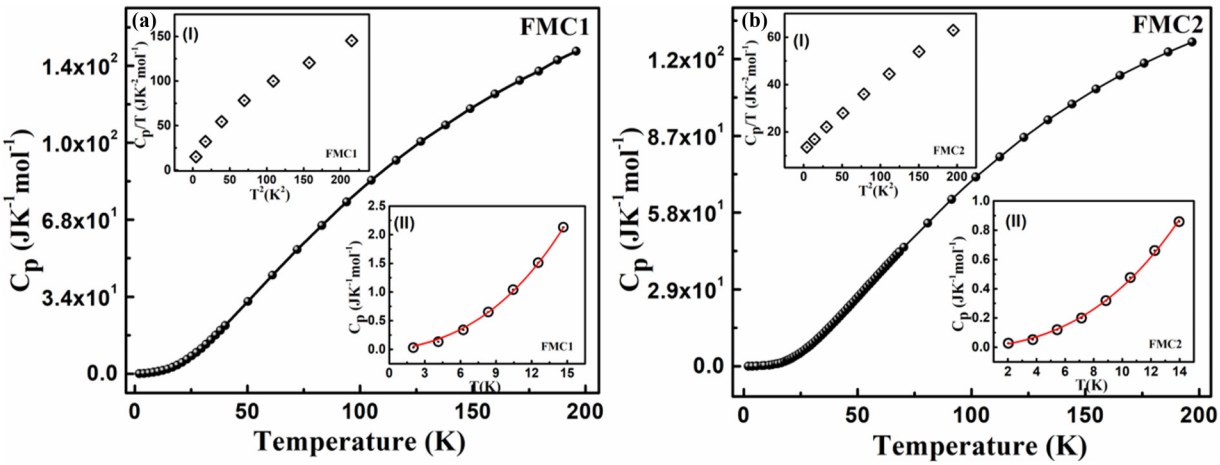

FIG. 9. Temperature evolution of heat capacity C_P in the presence of zero field: (a) FMC1 and (b) FMC2 [Insets: (I) C_P/T vs T^2, (II) C_P vs T and its fit to $C_p = \gamma T + \beta T^3$].

$M_{\text{max-FMC1}} = 0.44\,\mu_B$/f.u. and $M_{\text{max-FMC2}} = 0.28\,\mu_B$/f.u. The higher magnetization value obtained for FMC1 shows the existence of more FM cluster moment and weaker AFM interaction in FMC1. The coercivity values at 5 K are $H_{\text{C-FMC1}} = 6.84$ kOe and $H_{\text{C-FMC2}} = 5.11$ kOe. Large coercivity in both the compounds arises due to single-ion anisotropy of Co^{2+} ions and the presence of frozen spin clusters as well as AFM regions, which act as pinning

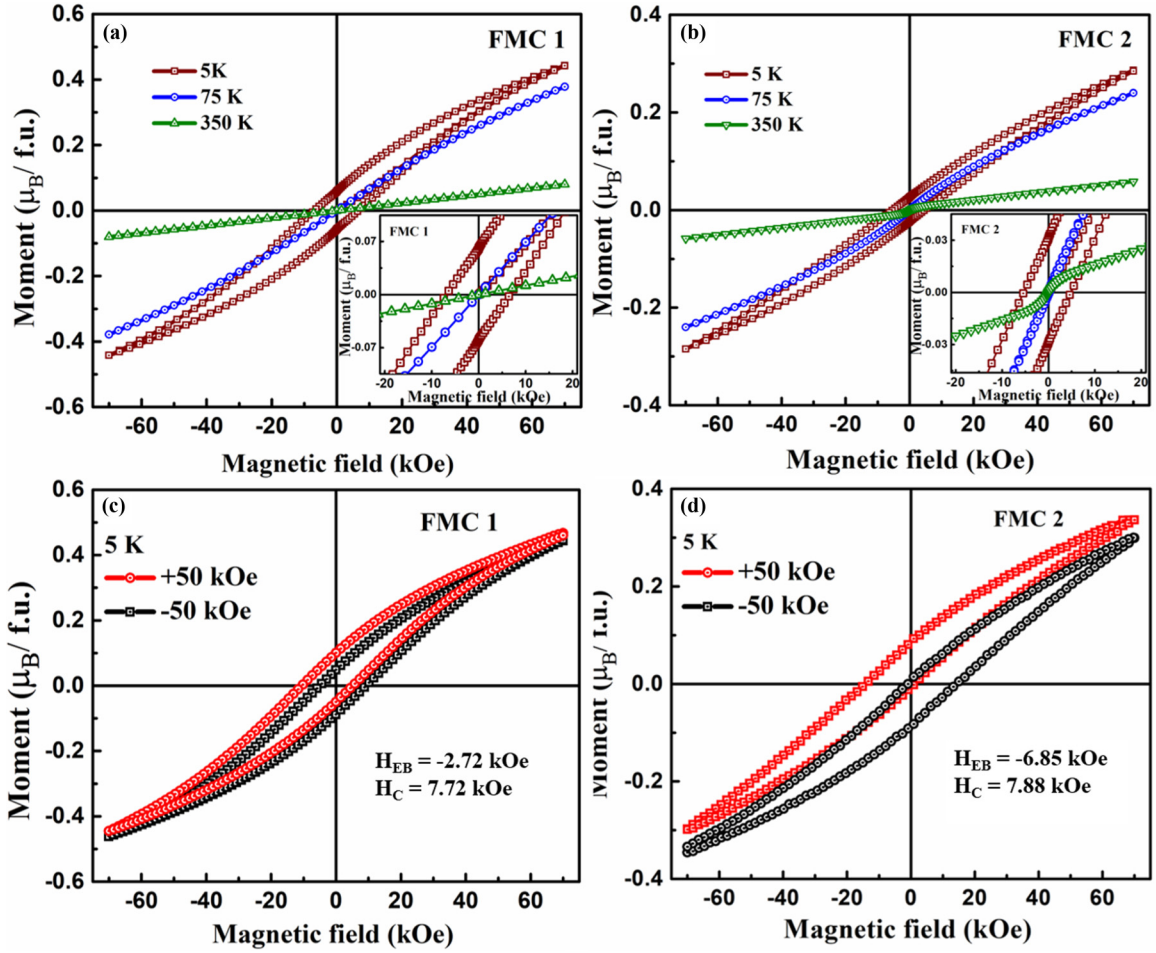

FIG. 10. Magnetization hysteresis loops of (a) FMC1 and (b) FMC2 under ZFC protocol at different temperatures. Hysteresis loops recorded under FC protocol for (c) FMC1 and (d) FMC2 at 5 K. Cooling field of +50 kOe and −50 kOe were applied in the FC protocol. Obtained EB and coercive fields are also mentioned.

centers to domain wall motion [64,65]. Enlarged loops of both compounds are shown in the inset of Figs. 10(a) and 10(b), which shows minor coercivity in FMC1 (26.3 Oe) and slightly enhanced coercivity in FMC2 (182.34 Oe) at 75 K. Further at 350 K, M(H) of FMC1 is a straight line, whereas FMC2 exhibits a linear dependence with "S" shape near the origin. Thus the enhanced coercivity at 75 K as well as the "S" shape of M(H) near the origin at 350 K in FMC2 points to the coexistence of short-range AFM and FM interactions in FMC2 even at higher temperatures. As a result, FMC2 is not completely paramagnetic even above T_2 which is further confirmed from the temperature variation of inverse susceptibility curve (given in Fig. S4 of the Supplemental Material [75]), similar features are reported for materials with short-range magnetic correlations above magnetic transition [66,67].

The coexistence of different magnetic phases such as FM, AFM or cluster glass may produce spin-disordered interfaces leading to the EB effect. To check the presence of EB, FC-M(H) measurements at 5 K have been carried out for both compounds after cooling them in an applied field of +50 kOe. Hysteresis loops obtained after field cooling were found to be asymmetric with a shift opposite to cooling field direction, as shown in Figs. 10(c) and 10(d) for FMC1 and FMC2, respectively. Further, the M(H) loop was measured for both samples at 5 K in a cooling field of −50 kOe, which shows hysteresis loop shift towards the positive field direction. In both the compounds, the M(H) loops recorded under ZFC protocol are centered at zero field and those measured in the FC protocol are shifted to the opposite direction of the applied cooling field of same amplitude, indicating that the shift observed in M(H) is intrinsic and is occurring due to the EB effect. For quantitative analysis of EB effects, EB and coercive fields are measured as

$$H_{\mathrm{EB}} = \frac{H_{C1} + H_{C2}}{2}, \tag{3}$$

$$H_C = \frac{|H_{c1}| + |H_{c2}|}{2}, \tag{4}$$

respectively, where H_{C1} is the left coercive field and H_{C2} is the right coercive field. Giant EB field values obtained for FMC1 and FMC2 at 5 K in +50 kOe cooling field are $H_{\mathrm{EB}} = -2.72$ kOe and $H_{\mathrm{EB}} = -6.85$ kOe, respectively, and the enhanced coercivity values for FMC1 and FMC2 are $H_{\mathrm{C}} = 7.88$ kOe and $H_{\mathrm{C}} = 7.72$ kOe, respectively. Even though the coercive field value is observed to be higher for FMC1, the EB value is observed to be larger for FMC2 and is higher than the values reported so far in any layered perovskite systems [17], to the best of our knowledge.

Another important feature observed in FC M(H) loops is the presence of large vertical shifts along with horizontal shifts. To quantify the asymmetry due to FC vertical shift compared to ZFC, we use the remanent magnetization values of the FC hysteresis loop. Hence we adopt the following formulas corresponding to the EB field and coercive field as, M_{EB} ($M_{\mathrm{EB}} = \frac{M_{\mathrm{C1}}+M_{\mathrm{C2}}}{2}$) and M_{C} ($M_{\mathrm{C}} = \frac{|M_{c1}|+|M_{c2}|}{2}$) to quantify the vertical shift and remanent asymmetry, which are considered as the equivalent parameters along the magnetization axis similar to H_{EB} and H_{C} [68]. The values of M_{EB} and M_{C} at 50 kOe are 0.027 μ_{B}/f.u., 0.08 μ_{B}/f.u, and 0.029 μ_{B}/f.u., 0.03 μ_{B}/f.u for FMC1 and FMC2, respectively.

The magnetic training effect is another signature of EB materials in which H_{EB} and H_{C} values exhibit a dramatic reduction as the material is continuously field cycled at a particular temperature. It manifests the irreversible changes of spins occurring at the interfaces (pinning boundaries) when the system undergoes consecutive field cycling [69]. Both FMC1 and FMC2 exhibit training effect when consecutive hysteresis loops were recorded at 5 K with a cooling field of 50 kOe. An abrupt change in H_{EB} was found after the first loop measurement as shown in Figs. 11(a) and 11(b) for FMC1 and FMC2, respectively. An enlarged view of the left side of hysteresis curves (near the Y axis = 0) are shown in inset I of both Figs. 11(a) and 11(b).

The power law fitting, in which the AFM moments at the interfaces are considered to undergo rearrangement, was done for the EB field, given by

$$H_{\mathrm{EB}}^{n} - H_{\mathrm{EB}}^{\infty} = \frac{k}{\sqrt{n}} \quad (n > 1), \tag{5}$$

where n is the number of consecutive cycles, k is a system dependent constant, H_{EB}^{n} and H_{EB}^{∞} are the EB field in the nth cycle and in the limit of infinite loops, respectively [69]. Solid curves in Figs. 11(a) and 11(b) represents the fit to Eq. (5) and the obtained fit parameters are $H_{\mathrm{EB}}^{\infty} = 1.15$ kOe, $k = 1.18$ kOe and $H_{\mathrm{EB}}^{\infty} = 3.78$ kOe, $k = 2.21$ kOe for FMC1 and FMC2, respectively. We note that, the experimental values of the EB field corresponding to $n = 1$ of FMC1 and FMC2, $-H_{\mathrm{EB}}^{1} = 2.72$ kOe and 6.85 kOe respectively, surpass the values calculated using Eq. (5) for $n = 1$ ($-H_{\mathrm{EB}}^{1} = 2.33$ kOe and 5.99 kOe). Thus calculated values for $n = 1$ using Eq. (5) confirms that the equation is only applicable for $n > 1$. A recursive formula was proposed by Binek [70] for the training effect, which we adopted for fitting the training effect for $n \geqslant 1$. According to this model, a thermodynamic framework of spin relaxation was considered for the AFM spins in the interface and the EB field in the $(n+1)^{\mathrm{th}}$ cycle is given by

$$H_{\mathrm{EB}}(n+1) = H_{\mathrm{EB}}(n) - \gamma\left[\left(H_{\mathrm{EB}}(n) - H_{\mathrm{EB}}^{\infty}\right)^{3}\right], \tag{6}$$

where $H_{\mathrm{EB}}(n)$ and H_{EB}^{∞} are the EB field in the nth cycle and in the limit of infinite loops, respectively, and γ is a system dependent constant. The parameters obtained from the best fit of the data to Eq. (6) are $\gamma = 0.1368 \pm 0.0082$ (10^{-2} Oe^{-2}), $H_{\mathrm{EB}}^{\infty} = 0.9692 \pm 0.0322$ kOe, and $\gamma = 0.0362 \pm 0.0022$ (10^{-2} Oe^{-2}), $H_{\mathrm{EB}}^{\infty} = 3.3966 \pm 0.0661$ kOe for FMC1 and FMC2, respectively. Further, from these values of γ, H_{EB}^{∞} and $H_{\mathrm{EB}}(1)$, H_{EB} was calculated for $n \geqslant 2$ [solid squares in the inset II of Figs. 11(a) and 11(b)], using Eq. (6). This confirms that the experimental values of the EB field at consecutive cycles are consistent with those obtained from the recursive formula in the Binek model. Further, we tried to fit the training effect data with another model proposed by Mishra *et al.* [71], in which the EB field in the nth cycle is given by

$$H_{\mathrm{EB}}^{n} = H_{\mathrm{EB}}^{\infty} + A_f \exp\left[\frac{-n}{P_f}\right] + A_r \exp\left[\frac{-n}{P_r}\right], \tag{7}$$

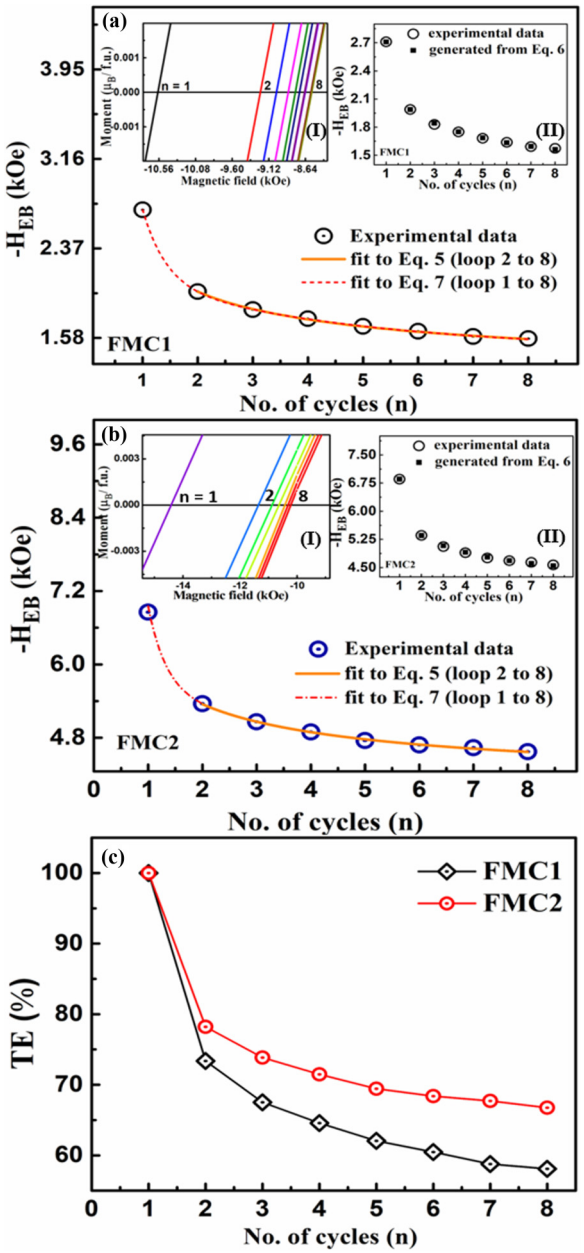

FIG. 11. Training effect in (a) FMC1 and (b) FMC2 in terms of the EB field at 5 K, (Inset I, Enlarged view of the left side of hysteresis curves (near the Y axis = 0) for different loop index n. Inset II, H_{EB} vs loop index n with the experimental data points (empty black circle) and data points (black solid square) generated from Eq. (6). The fit of Eqs. (5) and (7) are shown as a purple solid line and red dotted line, respectively. (c) Variation of TE[%] with the loop index n for FMC1 and FMC2 (data represented as open symbols with dot center connected by solid line).

where H_{EB}^{∞} is the EB field in the limit of infinite loops, A_f, P_f and A_r, P_r are parameters representing the frozen and rotatable spin moments in the pinning layer at the interface. P_f and P_r are dimensionless quantities related to the relaxation process (resemble the relaxation time), whereas A_f and A_r possess the dimensions of the magnetic field. According to the above model [Eq. (7)], two types of spins are present at the FM/AFM interfaces, frozen and rotating spins, resulting from the AFM anisotropy driven spin frustrations at the interface [68]. Both frozen and rotating spins are assumed to be exchange coupled to the FM/AFM regions.

A satisfactory fit was yielded with the parameters $H_{EB}^{\infty} = 1.46$ kOe, $A_f = 6.8$ kOe, $P_f = 0.42$, $A_r = 0.75$ kOe, $P_r = 4.12$ and $H_{EB}^{\infty} = 4.47$ kOe, $A_f = 2.95$ kOe, $P_f = 0.32$, $A_r = 1.63$ kOe, $P_r = 2.89$ for FMC1 and FMC2, respectively as shown in Figs. 11(a) and 11(b). The obtained parameters point to a greater contribution from the uncompensated rotating spins compared to the slowly relaxing frozen spins towards the reduction of EB field upon field cycling. The rotating spin component in FMC1 was found to relax ten times faster than the frozen component, whereas the same in FMC2 was found nine times faster. The relative percentage of reduction in EB (training effect percentage, TE%) on reaching the nth cycle was estimated [Fig. 11(c)] using the relation [72]

$$\mathrm{TE}[\%] = \left[1 - \frac{\left(H_{EB}^{1} - H_{EB}^{n}\right)}{H_{EB}^{1}}\right] \times 100\%, \tag{8}$$

where H_{EB}^{1} and H_{EB}^{n} are the values of EB in the 1st and in the nth cycles. H_{EB}^{2} fields were found to be decreasing to 73 and 78% of their initial values in FMC1 and FMC2, respectively, as shown in Fig. 11(c). Spin rearrangements occurring at the interfaces after each cycle result in the decay of EB field. Variation in TE[%] with increase in the loop index shows that EB becomes nearly 57% and 68% of their initial values (H_{EB}^{1}) for FMC1 and FMC2, respectively, after the 8th cycle, which indicates slightly more stable EB field in FMC2 compared to FMC1. The training effect data points of both FMC1 and FMC2 were fitted with the models proposed by Binek [70] as well as Mishra *et al.* [71] indicating the irreversible changes associated with the interface AFM spins as a result of consecutive field cycling.

I. Origin of exchange bias

To understand the origin of EB, temperature and cooling field dependence of EB fields (H_{EB} and M_{EB}) as well as coercive fields (H_C and M_C) have been studied and are summarized in Fig. 12. Thermal variation of H_{EB} measured below the T_1 transition temperature of FMC1 as well as FMC2 (in an applied field of 50 kOe) shows a significant increase of H_{EB}, H_C, M_{EB}, and M_C as shown in Fig. 12. The exponential decay of EB field as a function of temperature confirms the occurrence of spin frustration arising from competing magnetic interactions [73,74]. The temperature dependence of EB field in FMC1 and FMC2 was fitted [shown as solid lines in Figs. 12(a) and 12(b)] to the exponential relations

$$H_{EB} = H_{EB}^{0} \exp(-T/T_0), \tag{9}$$

$$M_{EB} = M_{EB}^{0} \exp(-T/T_*), \tag{10}$$

where T_0 (T_*) is a constant and H_{EB}^{0} (M_{EB}^{0}) is the extrapolation of H_{EB} (M_{EB}) to the absolute zero temperature. Values of H_{EB}^{0}, M_{EB}^{0}, T_0, and T_* obtained from the fit are 10.71 ± 0.59 kOe, 0.049 ± 0.005 μ_B/f.u, 3.45 ± 0.22, 5.50 ± 0.56 and 14.96 ± 0.66 kOe, 0.056 ± 0.005 μ_B/f.u, 5.15 ± 0.33, 7.13 ± 0.95 for FMC1 and FMC2, respectively. The temperature variation of the EB field shows zero EB value above glass

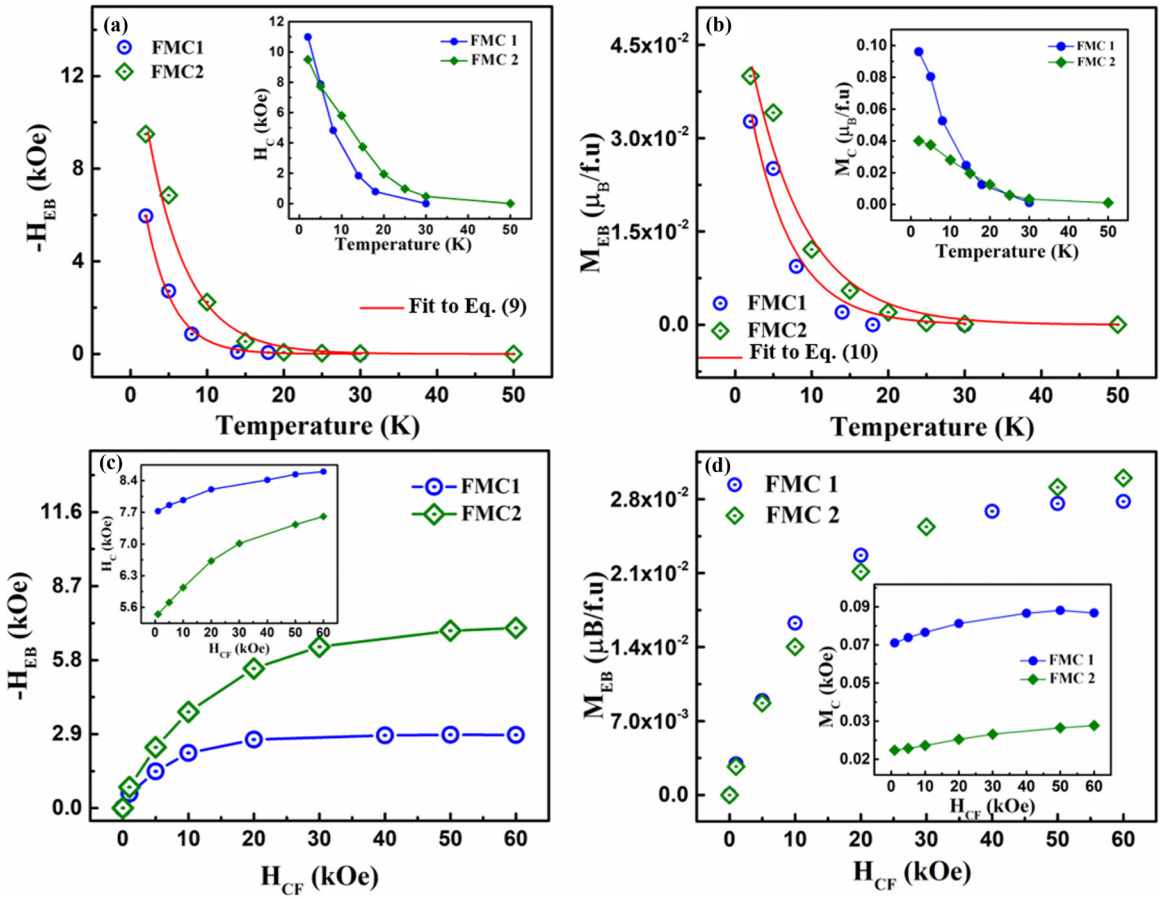

FIG. 12. (a) Temperature dependence of EB field H_{EB} (Inset shows temperature dependence of coercive field H_C) of FMC1 and FMC2. (b) Temperature dependence of EB field M_{EB} (Inset shows temperature dependence coercive field M_C) of FMC1 and FMC2 in FC protocol at an applied field of +50 kOe. Cooling field dependence of (c) H_{EB} and (d) M_{EB} at 5 K of FMC1 and FMC2, respectively.

transition (T_1) in both the compounds. This confirms that the origin of the EB in both the compounds is due to frozen spins, i.e., cluster glass phase. The sharp increase of EB field below T_1 (as shown in Fig. 12) can be attributed to the enhancement of magnetic irreversibility due to spin freezing [68]. At 2 K, FMC2 attains a giant EB value of 9.5 kOe, whereas FMC1 reaches to a 6 kOe EB field. However, rapid enhancement in H_C for FMC1 approaching ~11 kOe at 2 K was observed compared to FMC2, in which H_C of 9.2 kOe is attained at 2 K. The observed higher H_C confirms the presence of dominating FM clusters in FMC1. However, the higher EB obtained for FMC2 points to strong CG/AFM interface coupling in FMC2 compared to FMC1. The enhanced temperature dependence of H_C and M_C at lower temperatures arises from enhanced magnetization of FM clusters due to reduced thermal fluctuations. Further, H_{EB}, M_{EB}, H_C, and M_C increase in both the compounds as the cooling field (H_{CF}) increases as shown in Figs. 12(c) and 12(d). Both H_{EB} and H_C of FMC1 tend to saturate as the cooling field reaches 40 kOe, whereas the higher cooling field is required for FMC2, as H_{EB} does not saturate even at a cooling field of 60 kOe.

An intuitive illustration of the magnetic phase at 5 K, based on DC magnetization curves as well as M(H) isotherms, for FMC1 and FMC2 is shown in Figs. 13(a) and 13(b), respectively. Our experimental results confirm the coexistence of FM and AFM phases in FMC1 as well as in FMC2. The random occupancy of mixed-valent magnetic ions (Fe^{3+}/Fe^{4+}, Mn^{3+}/Mn^{4+}, Co^{2+}/Co^{3+}) at the magnetic perovskite layer give rise to locally varying competing AFM and FM exchange interactions, which produce cluster glass magnetic state ($T < T_1$) in both the compounds. The Fe-rich FMC2 possesses stronger AFM interactions due to dominant Fe-O-Fe superexchange interactions. However, in FMC1, the dominating Co-rich regions result in the reduction of AFM contributions. Since the EB effect in both the compounds is observed only below T_1, the cluster glass phase will be the source of origin. Thus, we assume the low temperature CG phase consists of FM and AFM regions, depicted as green and blue areas, respectively, in Fig. 13. The higher value of magnetization, as well as coercivity of FMC1, indicates more FM contribution, whereas the lower values of the same along with higher Fe content in FMC2 indicates more AFM regions in FMC2. There might be two possible origins of the EB effect; (i) CG spins pinned to the AFM regions (located at the boundaries of AFM regions) and (ii) FM spins that are pinned to the surrounding CG spins. As H_{CF} increases, the FM regions grow in size, i.e., more FM spins align along the field direction due to Zeeman coupling [68], and local anisotropy associated with the large FM region leads to an enhanced coercive field. The higher value of H_{EB} as well as

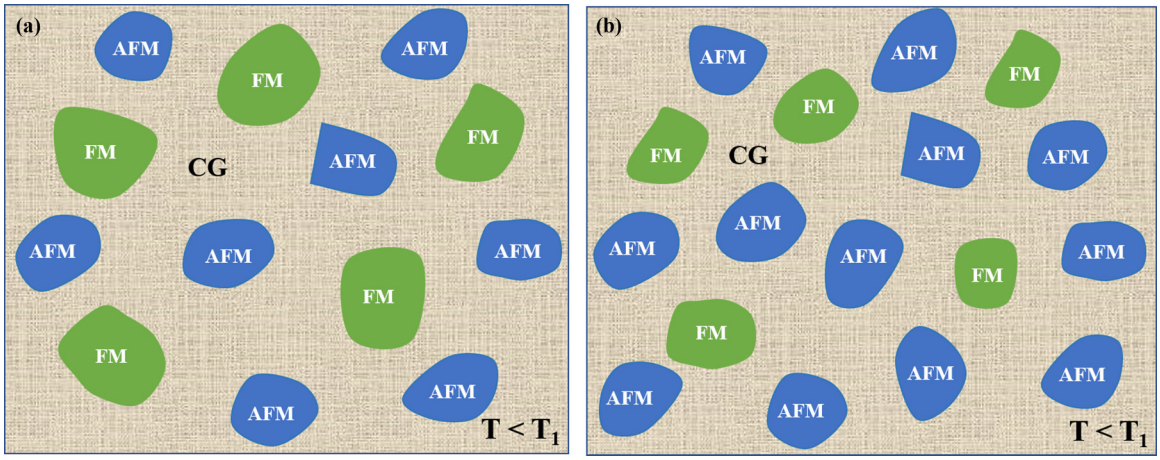

FIG. 13. Simplified schematic illustration of the inhomogeneous magnetic phase below cluster glass transition in (a) FMC1 and (b) FMC2. FM, AFM, and CG represent FM, AFM, and cluster glass regions respectively.

M_{EB} observed for FMC2 points to a higher number of pinned spins in FMC2 compared to FMC1 [73]. A plausible reason can be the presence of more AFM regions and stronger spin frustrations in FMC2. Also, H_{EB} does not tend to saturate even at a cooling field of 60 kOe in FMC2, which further confirms a higher fraction of strongly pinned spins in FMC2 compared to FMC1. Therefore, our results show that compositional tuning with the incorporation of multiple magnetic ions in the perovskite layers of RP structured compounds leads to atomic disorder induced strong exchange-coupling, enabling a control of the exchange bias.

IV. CONCLUSIONS

Phase pure quasi-2D single layer RP compounds FMC1 and FMC2 crystallize in tetragonal structure (space group *I4/mmm*) wherein FMC2 possesses 1.58% higher unit cell volume than FMC1. X-ray photoelectron spectroscopy confirms mixed valence states of Fe, Mn, and Co ions. Both compounds exhibit short-range AFM ordering at T_2 (∼297 K for FMC1 and ∼318 K for FMC2) followed by lower temperature cluster glass transition at $T_1 \sim 23$ K/43 K for FMC1/FMC2. Magnetic memory analysis together with AC susceptibility, NPD, and heat capacity studies, confirm the presence of a CG state below T_1, which arises due to competition between FM and AFM regions. Atomic disorder induced magnetic frustration, due to competition between FM-CG-AFM regions, is responsible for the evolution of giant EB of about 6 kOe and 9.5 kOe at 2 K in FMC1 and FMC2, respectively, for a cooling field of 50 kOe, which is the highest EB ever reported among any layered perovskite compounds, to the best of our knowledge. Further, our results provide an approach for designing of composition controlled quasi-2D layered perovskites with multiple magnetic ions at the B site towards tuning of EB. Importantly, EB in bulk materials due to competing magnetic interactions can be a positive approach towards the development of materials for the purpose of modern spintronic applications.

ACKNOWLEDGMENTS

P.N.S. acknowledges DST-SERB Project No. CRG/2018/003416 for financial support. P.N.L. acknowledges the Science and Engineering Research Board, India for National Post-Doctoral Fellowship No. PDF/2017/001826. A.V.K., P.N.L., R.D., and P.N.S. would like to acknowledge IITM for funding SVSM. The authors acknowledge DST FIST-Phase II funding for the PPMS (SR/FST/PSII-038/2016).

[1] S. Vasala and M. Karppinen, Prog. Solid State Chem. **43**, 1 (2015).
[2] K.-I. Kobayashi, T. Kimura, H. Sawada, K. Terakura, and Y. Tokura, Nature (London) **395**, 677 (1998).
[3] A. Filippetti and N. A. Hill, Phys. Rev. B **65**, 195120 (2002).
[4] D. Serrate, J. M. De Teresa1, and M. R. Ibarra, J. Phys.: Condens. Matter **19**, 023201 (2007).
[5] Y. Tokura and N. Nagaosa, Science **288**, 462 (2000).
[6] S. N. Ruddlesden and P. Popper, Acta Crystallogr. **10**, 538 (1957).
[7] V. L. Joseph Joly, P. A. Joy, S. K. Date, and C. S. Gopinath, Phys. Rev. B **65**, 184416 (2002).
[8] J. Nogués and I. K. Schuller, J. Magn. Magn. Mater. **192**, 203 (1999).
[9] J. Nogués, J. Sort, V. Langlais, V. Skumryev, S. Suriñach, J. Muñoz, and M. Baró, Phys. Rep. **422**, 65 (2005).
[10] M. Ali, P. Adie, C. H. Marrows, D. Greig, B. J. Hickey, and R. L. Stamps, Nat. Mater. **6**, 70 (2007).
[11] G. Wang, Y. Huang, S. Sun, J. Wang, R. Peng, and Y. Lu, J. Am. Ceram. Soc. **99**, 1318 (2016).

[12] V. Korenivski, R. B. van Dover, Y. Suzuki, E. M. Gyorgy, J. M. Phillips, and R. J. Felder, J. Appl. Phys. **79**, 5926 (1996).
[13] S. S. P. Parkin, K. P. Roche, M. G. Samant, P. M. Rice, and R. B. Beyers, J. Appl. Phys. **85**, 5828 (1999).
[14] J. Kools, IEEE Trans. Magn. **32**, 3165 (1996).
[15] S. A. Wolf, D. D. Awschalom, R. A. Buhrman, J. M. Daughton, S. von Molnár, M. L. Roukes, A. Y. Chtchelkanova, and D. M. Treger, Science **294**, 1488 (2001).
[16] K. Zhang, T. Zhao, and H. Fujiwara, J. Appl. Phys. **89**, 6910 (2001).
[17] R. R. Das, P. Parida, A. K. Bera, T. Chatterji, B. R. K. Nanda, and P. N. Santhosh, Phys. Rev. B **98**, 184417 (2018).
[18] G. R. Haripriya, C. M. N. Kumar, R. Pradheesh, L. M. Martinez, C. L. Saiz, S. R. Singamaneni, T. Chatterji, V. Sankaranarayanan, K. Sethupathi, B. Kiefer, and H. S. Nair, Phys. Rev. B **99**, 184411 (2019).
[19] R. C. Sahoo, Y. Takeuchi, A. Ohtomo, and Z. Hossain, Phys. Rev. B **100**, 214436 (2019).
[20] J. Rodriguez-Carvajal, Physica B **192**, 55 (1993).
[21] K. Momma and F. Izumi, J. Appl. Crystallogr. **44**, 1272 (2011).
[22] R. R. Das and C. V. Colin (unpublished).
[23] A. V. Chichev, M. Dlouhá, S. Vratislav, K. Knížek, J. Hejtmánek, M. Maryško, M. Veverka, Z. Jirák, N. O. Golosova, D. P. Kozlenko, and B. N. Savenko, Phys. Rev. B **74**, 134414 (2006).
[24] D. Singh, S. Singh, A. Mahajan, and N. Choudhary, Ceram. Int. **40**, 1183 (2014).
[25] A. Benabad, A. Daoudi, R. Salmon, and G. Le Flem, J. Solid State Chem. **22**, 121 (1977).
[26] R. D. Shannon, Acta Crystallogr. **A32**, 751 (1976).
[27] D. Senff, P. Reutler, M. Braden, O. Friedt, D. Bruns, A. Cousson, F. Bourée, M. Merz, B. Büchner, and A. Revcolevschi, Phys. Rev. B **71**, 024425 (2005).
[28] M. C. Biesinger, B. P. Payne, A. P. Grosvenor, L. W. M. Lau, A. R. Gerson, and R. S. C. Smart, Appl. Surf. Sci. **257**, 2717 (2011).
[29] Z. Yang, Z. Zhang, Y. Jiang, M. Chi, G. Nie, X. Lu, and C. Wang, RSC Adv. **6**, 33636 (2016).
[30] R. Li, C. Sun, J. Liu, and Q. Zhen, RSC Adv. **7**, 50546 (2017).
[31] J. Zhu, S. Guo, Z. Chu, and W. Jin, Mater. Chem. A **3**, 22564 (2015).
[32] M. Aronniemi, J. Sainio, and J. Lahtinen, Surf. Sci. **578**, 108 (2005).
[33] S. Arumugam, Y. Toku, and Y. Ju, Sci. Rep. **10**, 5407 (2020).
[34] H. Guo, Z. Hu, T.-W. Pi, L. H. Tjeng, and A. C. Komarek, Crystals **6**, 98 (2016).
[35] A. M. Durand, D. P. Belanger, C. H. Booth, F. Ye, S. Chi, J. A. Fernandez-Baca, and M. Bhat, J. Phys.: Condens. Matter **25**, 382203 (2013).
[36] A. Tabuchi, H. Kawanaka, H. Bando, T. Sasaki, and Y. Nishihar, J. Alloys Compd **424**, 21 (2006).
[37] K. Aso and S. Miyahara, J. Phy. Soc. Jpn. **21**, 1833 (1966).
[38] J. W. Seo, E. E. Fullerton, F. Nolting, A. Scholl, J. Fompeyrine, and J.-P. Locquet, J. Phys.: Condens. Matter **20**, 264014 (2008).
[39] K. Chandran, P. N. Lekshmi, and P. N. Santhosh, J. Solid State Chem. **279**, 120910 (2019).
[40] C. Gauvin-Ndiaye, A. M. S. Tremblay, and R. Nourafkan, Phys. Rev. B **99**, 125110 (2019).
[41] H. El Shinawi and C. Greaves, J. Solid State Chem. **181**, 2705 (2008).
[42] R. R. Das, P. N. Lekshmi, S. C. Das, and P. N. Santhosh, J. Alloys Compd. **773**, 770 (2019).
[43] L. Bufaiçal, R. Finkler, L. T. Coutrim, P. G. Pagliuso, C. Grossi, F. Stavale, E. Baggio-Saitovitch, and E. M. Bittar, J. Magn. Magn. Mater. **433**, 271 (2017).
[44] F. Wang, J. Zhang, Y.-F. Chen, G.-J. Wang, J.-R. Sun, S.-Y. Zhang, and B.-G. Shen, Phys. Rev. B **69**, 094424 (2004).
[45] R. S. Freitas and L. Ghivelder, F. Damay, F. Dias, and L. F. Cohen, Phys. Rev. B **64**, 144404 (2001).
[46] R. Pradheesh, H. S. Nair, G. R. Haripriya, A. Senyshyn, T. Chatterji, V. Sankaranarayanan, and K. Sethupathi, J. Phys.: Condens. Matter **29**, 095801 (2017).
[47] M. Bandyopadhyay and S. Dattagupta, Phys. Rev. B **74**, 214410 (2006).
[48] V. Markovich, I. Fita, A. Wisniewski, G. Jung, D. Mogilyansky, R. Puzniak, L. Titelman, C. Martin, and G. Gorodetsky, Phys. Rev. B **81**, 134440 (2010).
[49] Y. Sun, M.B. Salamon, K. Garnier, and R. S. Averback, Phys. Rev. Lett. **91**, 167206 (2003).
[50] K. Yadav, M. K. Sharma, S. Singh, and K. Mukherjee, Sci. Rep. **9**, 15888 (2019).
[51] K. Binder and A. P. Young, Rev. Mod. Phys. **58**, 801 (1986).
[52] J. A. Mydosh, *Spin Glasses: An Experimental Introduction* (CRC Press, Boca Raton, FL, 2014).
[53] P. C. Hohenberg and B. I. Halperin, Rev. Mod. Phys. **49**, 435 (1977).
[54] M. D. Mukadam, S. M. Yusuf, P. Sharma, S. K. Kulshreshtha, and G. K. Dey, Phys. Rev. B **72**, 174408 (2005).
[55] H. Khurshid, P. Lampen-Kelley, O. Iglesias, J. Alonso, M. H. Phan, C. J. Sun, M. L. Saboungi, and H. Srikanth, Sci. Rep. **5**, 15054 (2015).
[56] J. Souletie and J. L. Tholence, Phys. Rev. B **32**, 516 (1985).
[57] S. Sabyasachi, M. Patra, S. Majumdar, S. Giri, S. Das, V. S. Amaral, O. Iglesias, W. Borghols, and T. Chatterji, Phys. Rev. B **86**, 104416 (2012).
[58] S. D. Bhame, V. L. Joseph Joly, and P. A. Joy, Phys. Rev. B **72**, 054426 (2005).
[59] N. Brahiti, M. Abbasi Eskandari, M. Balli, C. Gauvin-Ndiaye, R. Nourafkan, A. M. S. Tremblay, and P. Fournier, J. Appl. Phys. **127**, 113905 (2020).
[60] L. Ghivelder, I. A. Castillo, M. A. Gusmão, J. A. Alonso, and L. F. Cohen, Phys. Rev. B **60**, 12184 (1999).
[61] E. S. R. Gopal, *Specific Heats at Low Temperatures* (Plenum, New York, 1966).
[62] J. M. D. Coey, S. von Molnar, and R. J. Gambino, Solid State Commun. **24**, 167 (1977).
[63] J. O. Thomson and J. R. Thomson, J. Phys. F **11**, 247 (1981).
[64] N. Hollmann, M. W. Haverkort, M. Cwik, M. Benomar, M. Reuther, A. Tanaka, and T. Lorenz, New J. Phys. **10**, 023018 (2008).
[65] S. Mukherjee, R. Ranganathan, and P. Mondal, J. Phys. Chem. Solids **61**, 1433 (2000).
[66] D. Yang, T. Yang, P. Mukherjee, S. E. Dutton, D. Huo, and M. A. Carpenter, Phys. Rev. B **99**, 094314 (2019).
[67] R. Kamel, A. Tozri, E. Dhahri, and E. K. Hlil, RSC Adv. **9**, 27541 (2019).
[68] S. Karmakar, S. Taran, E. Bose, B. K. Chaudhuri, C. P. Sun, C. L. Huang, and H. D. Yang, Phys. Rev. B **77**, 144409 (2008).

[69] D. Paccard, C. Schlenker, O. Massenet, R. Montmory, and A. Yelon, Phys. Status Solidi **16**, 301 (1966).
[70] C. Binek, Phys. Rev. B **70**, 014421 (2004).
[71] S. K. Mishra, F. Radu, H. A. Dürr, and W. Eberhardt, Phys. Rev. Lett. **102**, 177208 (2009).
[72] J. Ventura, J. P. Araujo, J. B. Sousa, A. Veloso, and P. P. Freitas, Phys. Rev. B **77**, 184404 (2008).
[73] X. H. Huang, J. F. Ding, G. Q. Zhang, Y. Hou, Y. P. Yao, and X. G. Li, Phys. Rev. B **78**, 224408 (2008).
[74] N. Moutis, C. Christides, I. Panagiotopoulos, and D. Niarchos, Phys. Rev. B **64**, 094429 (2001).
[75] See Supplemental Material at http://link.aps.org/supplemental/10.1103/PhysRevB.102.134405 for variation of B-O_2 bond length for the $SrLaMO_4$ series of compounds, XPS core level spectra and fit for $2p_{1/2}$ lines, temperature evolution of magnetization of $SrLaFe_{0.5}Co_{0.5}O_4$ and inverse susceptibility curves of FMC1 and FMC2. Details of the NPD refinement are also tabulated.